Results in Engineering 29 (2026) 109642

Contents lists available at ScienceDirect

Results in Engineering

journal homepage: www.sciencedirect.com/journal/results-in-engineering

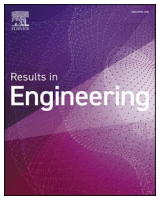

Research paper

Design of experiment assisted optimization of the bonding conditions of S235/TiAl6V4 composite

Fedor Levchenko [a,*], Thomas Gietzelt [a], Eero Scherman [b,c], Uta Gerhards [a], Volker Toth [a], Juha Pyrhönen [c], Martin Doppelbauer [a]

[a] Karlsruhe Institute of Technology, Hermann-von-Helmholtz-Platz 1, 76344 Eggenstein Leopoldshafen, Germany
[b] LAB University of Applied Sciences, Yliopistonkatu 36, 53850 Lappeenranta, Finland
[c] Lappeenranta-Lahti University of Technology, Yliopistonkatu 34, 53850 Lappeenranta, Finland

ARTICLE INFO

Keywords:
Diffusion bonding
Axially laminated rotor
ALA
Reluctance machine
SynRM
Design of experiments
Mild steel
S235
Titanium grade 5
TiAl6V4

ABSTRACT

In response to prevailing market demands with a view to reducing the carbon emissions, there is an increasing need for high-speed/high-power electrical machines. The synchronous reluctance machine (SRM) with an axially laminated rotor (ALA) is a relatively old concept, which has recently attracted renewed interest due to the new technological possibilities. It is considered a promising candidate for high-power applications. However, the optimal combination of materials for an ALA composite remains to be identified. The present paper focuses on a novel combination of materials for this application: titanium grade 5 (TiAl6V4) with mild steel (S235). The application of diffusion bonding can help with reliable joining of dissimilar materials; nevertheless, the optimisation of the bonding parameters remains a challenging aspect. Several studies have addressed the diffusion bonding of titanium with various alloys; however, it remains unclear, which combination of parameters (time, temperature, and pressure) yields the highest mechanical strength. In this work, experimental design (DoE) method was employed to evaluate these parameters, with the shear strength serving as a primary response. For understanding, how the bonding parameters affect the microstructure, scanning electron microscopy (SEM) was used. It was found that at the 95% confidence level, temperature was the only variable that maintained its statistical significance. The maximum shear strength was observed in joints, welded at 900°C, in agreement with the predictions of the DoE model.

1. Introduction

The necessity for high-power machines [1] can be fulfilled by utilizing a solid rotor with exceptional mechanical strength [2] and a high rotational speed. Rotors with an axially laminated anisotropic (ALA) structure (see Fig. 1) are good candidates. However, an ALA rotor, requires the bonding of two distinct materials: soft-magnetic (serving as flux guides) and non-magnetic (serving as flux barrier). Most research and development in this field has focused on the bonding of metals, which is also the case in manufacturing of bulk material for an ALA rotor.

Ferromagnetic steels are generally used as soft-magnetic materials. One of the problems related to solid rotor constructions is that air gap permeance and stator harmonics create significant eddy-current losses on the surface of the solid rotor. Therefore, to eliminate the eddy-currents, it would be optimal to select for the non-magnetic layer an electrically non-conductive material. Due to the high temperatures used in diffusion bonding (DB), such materials could be, for example, ceramics or single-crystal inorganic oxides or nitrides. However, the process of forming bonds between ceramics and metals is challenging [3]. It is anticipated that the issue of eddy current elimination will be addressed by electrical engineers, who design the stator for a given rotor geometry. Consequently, a non-magnetic metal is typically employed as a flux barrier material.

According to Credo [4] et al. from an electromagnetic perspective TiAl6V4 is considered as the optimal candidate for utilisation as a non-magnetic material, due to its low density, outstanding mechanical properties, and high electrical resistivity, which help to diminish the eddy-current losses. The initial assumption regarding the magnetic layer was that S235 would be a suitable material due to the following reasons:

* Corresponding author.
E-mail addresses: fedor.levchenko@kit.edu (F. Levchenko), thomas.gietzelt@kit.edu (T. Gietzelt), eero.scherman@lab.fi (E. Scherman), uta.gerhards@kit.edu (U. Gerhards), volker.toth@kit.edu (V. Toth), juha.pyrhonen@lut.fi (J. Pyrhönen), martin.doppelbauer@kit.edu (M. Doppelbauer).

https://doi.org/10.1016/j.rineng.2026.109642
Received 27 March 2025; Received in revised form 17 February 2026; Accepted 17 February 2026
Available online 18 February 2026

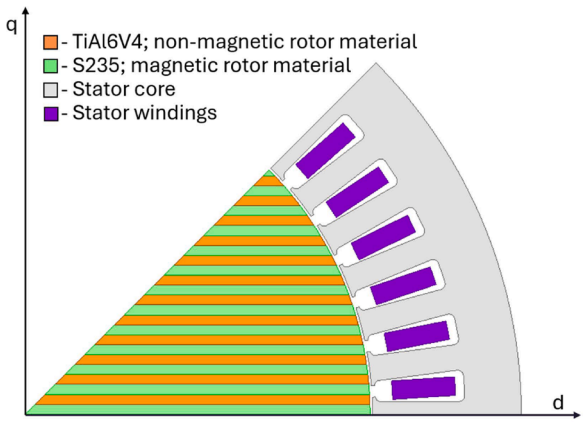

Fig. 1. A 1/8 piece of the two-pole ALA rotor for SynRM; q - quadrature axis, d – direct axis.

low cost, accessibility in many dimensions and relatively high saturation magnetization. The primary issues associated with mild steel S235 are its high thermal expansion coefficient (compared to TiAl6V4) and its poor mechanical properties. Another challenge when working with Ti-6Al-4V is its poor machinability [5]. Conversely, the utilisation of cold-rolled steels is insufficient, given that DB necessitates temperatures higher than 700°C, which eliminate all cold-working effects. The bonding of titanium with steel parts is a common practice in the aerospace industry [6,7], with the hot isostatic pressing method being particularly prevalent due to its ability to accommodate more sophisticated geometries [8]. In this study, the uniaxial DB method was employed as the primary investigative approach.

Diffusion bonding is one of several techniques used to join dissimilar materials. Alternative methods include vacuum brazing or explosion welding [9,10] as well as hot isostatic pressing [11]. Additive manufacturing has also been explored for this purpose [12–14]. Among these approaches, DB enables the joining of a wide range of dissimilar materials and is generally simpler and more cost-effective than the other techniques.

The diffusion process, in general, can be described by the second Fick's law:

$$\frac{\partial C}{\partial t} = D\frac{\partial^2 C}{\partial x^2}, \tag{1}$$

Where C is the concentration as a function of time t and distance from the bonding interface x, and D is the diffusion coefficient, which is a temperature-dependent material property, given by Arrhenius law:

$$D = D_0 \exp\left(-\frac{E_A}{RT}\right), \tag{2}$$

Where D_0 is the initial diffusion coefficient, E_A is the activation energy for diffusion, R is the universal gas constant and T is the temperature. Assuming that, the diffusion driving forces can be divided into two parts: thermodynamic (temperature-dependent) and kinetic (time-dependent). As will be shown below, both parts may play a crucial role in diffusion bonding, determining the final quality of the bond formed between the materials. Moreover, the formation of new phases at the bonding interface, may also be thermodynamically or kinetically driven. Together, thermodynamics and kinetics determine the conditions needed for effective diffusion bonding and the quality of the resulting bond.

A further factor to be considered is the chemical composition of both materials. First, it is worth noting that although TiAl6V4 naturally contains up to 0.4% iron, titanium can form brittle intermetallic compounds with iron. Second, carbon atoms can diffuse into the titanium alloy, forming various carbides, which may also affect the final bond strength. Moreover, both materials undergo phase transitions [15,16]:

$$\text{For S235}: \alpha_{bcc} \xrightarrow{\approx 800^\circ C} \gamma_{fcc}$$

$$\text{For TiAl6V4}: \alpha_{hcp} + \beta_{bcc} \xrightarrow{\approx 900^\circ C} \beta_{bcc}$$

These transitions lead to different inter-diffusion coefficients [17], which are temperature-dependent. Consequently, the behaviour of the bonding interface in general becomes much more complex, due to heating and cooling during the whole process. Furthermore, it is necessary to consider not only the thermodynamic perspective, but also the possibility of avoiding the formation of brittle intermetallic phases, as proposed in [18], by utilizing a brief holding time for the process e.g. kinetics, which is hardly applicable the in case of diffusion bonding furnace without induction heating.

Due to the abovementioned reasons, choosing the right combination of process parameters (dwell time, temperature and contact pressure) is quite challenging. Unsurprisingly, the literature reveals a considerable range of parameters employed by different authors when welding TiAl6V4 alloy: the temperature range spans from 650°C to 950°C [19,20], the pressure ranges from 0.5 MPa to 30 MPa [21,22], and the process time ranges from 10 minutes to 3 hours [21,23]. Notably, most of these publications consider austenitic stainless steels as a pair for TiAl6V4 alloy [24–26], (which is not magnetic and additionally contain nickel and chromium) and sometimes consider using an interlayer [23,27,28].

In most of the abovementioned articles, the authors vary only one bonding parameter (typically temperature), which doesn't give a full view of the process. Moreover, different diffusion bonding furnaces have different heating systems, which makes it impossible to compare the results directly. For now, the most comprehensive analysis has been conducted by *Negemiya et al* [29], where all three parameters were varied at five levels, but for the TiAl6V4/AISI304 material pair.

The present article, however, focuses on the welding of TiAl6V4 with ferromagnetic S235, which is crucial for SynRelALA applications. No interlayer was used to understand how the diffusion bonding conditions affect the kinetics and thermodynamics of the intermetallic phase formation. The initial assumption was, that low-temperature condition would supress the formation of brittle phases, on the other hand the temperature must be high enough to activate diffusion process. However, it is assumed that the presence of the intermetallic phase will limit the mechanical strength of the joint.

The abovementioned reasons emphasise the necessity of selecting an appropriate evaluation method to ascertain the optimal bonding conditions. To achieve this, the design of experiments method, described in the next section, was employed (the same method was as in [29]). Afterwards the bonding interface characterization is presented, followed by a section in which the shear strength of the joints was measured. Based on those results, in the last section, the DoE model is constructed.

2. Materials and methods

The rotatable orthogonal central composite design (ROCCD) was used for the planning of the experiments. After performing the experiments, the Least-Mean-Squares-Algorithm was used to build the equation for the response surface. Then using the Student t-test, the non-significant factors were excluded.

All experiments were conducted in a diffusion bonding furnace manufactured by MAYTEC with a maximum load of 20 kN at an accuracy of 1% and an average cooling rate of 6.1 K min^{-1} from 1100 to 300°C. To achieve adequate the proper surface purity (and to remove the oxide layer on TiAl6V4) all experiments were carried out in high vacuum in the range of 10^{-5} mbar (more information about the vacuum-quality-preservation see [30]). The metallic molybdenum heaters of the furnace heated the billet by IR radiation. The heating rate was about 10

K min^{-1} [30]. The furnace was equipped with a thermocouple of type S (Pt10%Rh-Pt), class 1 with an accuracy of $\pm(1+0.003\cdot(t-1100))$ K in a range $T \in [273;\ 1873]$ K. At the beginning, a preload of 0.5 kN was applied, and after the heating to the desired temperature, the full load was applied [30].

2 mm thick sheets of both S235 and TiAl6V4 were chosen as starting materials. The chemical composition of the parent materials, given by the manufacturer, is shown in Table 1:

After diffusion bonding, cross-sections of the samples were prepared and examined using a Jeol JXA 8530-F field emission microprobe. Each sample was first grinded with SiC-sandpapers P600/1200/2000 and polished afterwards using diamond suspension 3/1 μm, afterwards the specimens were placed in Epofix epoxy resin. SEM-BSE images were taken and the corresponding WDS elemental maps of the main elements in the diffusion zones were recorded at 15 kV and 20 nA. The same device was used for the quantitative analysis to determine the composition of individual phases in the parent materials. Kα emission lines were checked to identify the quantitative chemical composition for Ti, Al, Fe, C and Mn except V, where the Kβ emission line was used (since the Kβ line of Ti is very close to the Kα line of V, it is hard to distinguish them).

The shear strength was measured with a universal testing machine (Matertest Oy FMT-250, Finland) equipped with a test device to induce shear stress on the samples. The shear strength tests were completed in a similar manner to that described in [10].

2.1. Planning of the experiment

For the preliminary understanding of the behaviour of the joint between Ti and S235 a few initial experiments were made. From both S235 and TiAl6V4 squared pieces 30 × 30 × 2 mm^3 were cut. For the diffusion bonding experiments a layer of TiAl6V4 was located between two S235 pieces. The sample geometry for all cases is illustrated in Fig. 2:

As mentioned in the previous section, based on the available literature, it was decided to use average values for the time, temperature and pressure. However, a few preliminary experiments were required to understand if the chosen levels were adequate. Thus, the first experiment was conducted with the following parameters: temperature of 900°C, contact pressure 32 of MPa and dwell time 60 of min. It was found that TiAl6V4 exhibited a much more severe plastic deformation than S235under elevated temperatures [29], moreover the deformation in the bonding direction under the abovementioned conditions was about 13%, whereas the acceptable level of deformation is normally up to 5%. That indicated that the chosen contact pressure level was higher than required. However, the joint in general did not break during the machining, which indicated, that the values of time and temperature were chosen correctly.

A follow-up experiment employed reduced pressure to avoid excessive deformation and a lower bonding temperature (732°C, 15 MPa and 60 min). The resulting specimen exhibited negligible deformation but fractured after bonding, implying that the temperature was inadequate for effective joint formation.

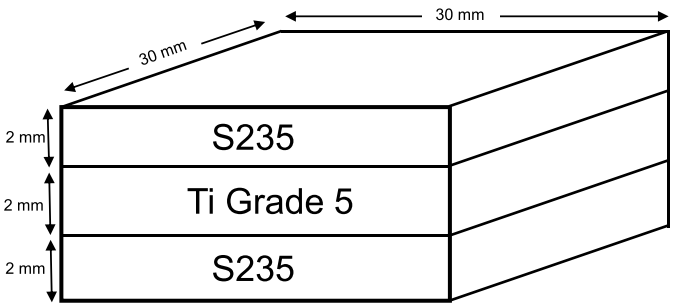

Fig. 2. Samples geometry.

Based on the preliminary results above, it was decided to set the "zero levels" of the DB parameters at the following values: 15 MPa for the contact pressure, 900°C for the temperature and 60 min for the dwell time. The differences between the levels were chosen in such a way that the calculated "star points" were at adequate level, while ensuring that the levels were not too far away from each other. It is important to note that even a 50 K difference in the bonding temperature may be crucial because of the kinetics and thermodynamics of the phase transformations, described in the first section.

Based on this assumption, the experiment plan using a rotatable orthogonal central composite design (ROCCD), as an optimal 2nd order design, which allows to obtain the homogeneously distributed information from the response surface [31] was created. see Table 2:

The shear strength was used as a key parameter, to be analysed and maximized. In accordance with the theory, a total of 15 different experiments need to be made (including one "zero point" and six "star points"), using the formulas given by DoE theory [32]:

$$N = 2^n + 2n + n_0' \tag{3}$$

In this context, the value of n represented the number of factors, which in this case was equal to three. The value of n_0' was the number of experiments at the "zero point", which can be derived for ROCCD using the formula [32]:

$n_0' = 4 - 2n + 2^{\frac{n+4}{2}} = 9,314$ for $n = 3$. Rounding down in total 9 experiments at "zero point" should have been performed, but for simplicity only one experiment was conducted at that point, with all

Table 2
Levels of the factors in the diffusion bonding process between TiAl6V4 and S235.

	-1.682	-1	0	1	1.682
p (MPa)	10	12	15	18	20
T (°C)	816	850	900	950	984
t (min)	10	30	60	90	110

Table 1
Chemical compositions of S235 and TiAl6V4.

TiAl6V4								
Element	Ti	Al	V	Fe	O	C	N	H
wt-%	Balance	5.50 - 6.75	3.50 - 4.50	≤ 0.40	≤ 0.20	≤ 0.40	≤ 0.05	≤ 0.015
S235								
Element	Fe		Mn	C	Si	P	S	Cu
wt-%	Balance		≤ 1.60	≤ 0.22	≤ 0.05	≤ 0.05	≤ 0.05	≤ 0.55

The surface quality of the parent materials was measured by a Sensofar SM6V6 REV1 interferometer using a 10^x zooming lens: $R_a^{S235} = 1.5$ μm, $R_a^{TiAl6V4} = 0.7$ μm. This was considered acceptable for the diffusion bonding experiments. Before the DB, the surfaces of both metals were grinded with a SiC-sandpaper P600 and afterwards sonicated in and rinsed with isopropanol.

nine rows filled with the same value of the shear strength (assuming, that normally diffusion bonding provides highly reproducible results). For calculation of the "star points" the following expression was used [32]:

$$\alpha^* = 2^{\frac{n}{4}} \quad (4)$$

The experimental design is shown in Table 3. The initial eight experiments were conducted at the corners of the cube, whereas the subsequent seven experiments were carried out at the "star points". The final experiment was conducted at the "zero point". To avoid a systematic error, the experiments were performed in a random order.

The data presented in this table served as the basis for all subsequent experiments. The experiments described above (sample #1: 900°C, 32 MPa, 60 min and sample #4: 732°C, 15 MPa, 60 min) were not included in the plan. Table 3 also presents the values of the relative deformation.

Clear trends in deformation were observed (see Fig. 3): Increasing temperature, pressure or time of diffusion bonding led to increased deformation. While deformation increased linearly with time, its response to variations in temperature and pressure was non-linear. This behaviour can be attributed to the high plasticity of TiAl6V4 at elevated temperatures; even 450°C [33] is sufficient to activate this mechanism. This is further supported by Norton's law: $\dot{\varepsilon} = A\sigma^n \exp(-\dot{\varepsilon}/RT)$, where $\dot{\varepsilon}$ is deformation rate, σ is applied stress, Q is activation energy, T is temperature and A and n are material constants. The equation clearly illustrates the non-linear dependence of deformation rate on both pressure and temperature.

2.2. SEM of initial materials

To understand the bond formation processes, the SEM images of the joints were acquired. For chemical characterization EDS and WDS were used. First, SEM images of the initial structures of TiAl6V4 and S235 were obtained, see Fig. 4:

The structures of both initial materials were homogeneous. As mentioned in Section 1, titanium alloy contains two phases, which can be observed as light and dark regions in Fig. 4. α-phase has a hexagonal close-packed (HCP) crystal structure, whereas β-phase has a body-centred cubic (BCC) structure that is stable at higher temperatures in pure Ti. With the help of Electron Probe Micro Analysis (EPMA) the chemical compositions of both phases were measured, see Table 4:

Alloying elements in titanium alloys influence the stability of the α and β phases [17]. In this study, V and Fe act as β stabilizers, while Al stabilizes the α phase, resulting in elemental segregation between the phases. On this basis, and in agreement with SEM contrast principles, the darker contrast is attributed to the α phase and the brighter contrast to the β phase.

Table 3
Rotatable orthogonal central composite design.

p (MPa)	T (°C)	t (min)	Sample #	Deformation%
12	850	30	9	1.49
18	850	30	11	4.81
12	950	30	10	2.54
18	950	30	12	4.76
12	850	90	13	3.67
18	850	90	14	13.02
12	950	90	15	4.32
18	950	90	16	10.89
10	900	60	17	1.83
20	900	60	2	6.70
15	816	60	7	2.17
15	984	60	8	6.52
15	900	10	5	0.75
15	900	110	6	4.96
15	900	60	3	2.89

2.3. SEM of the bonded samples

In the same way, SEM images of all bonded samples were acquired, although only images of selected samples are shown.

In general, the SEM images of the samples could be divided into three groups: A, B and C, as shown in Table 5. Noteworthy, the temperature of diffusion bonding fully determined each group. Samples #4 and #7 were not included in Table 5, because, for them, the bond was too weak, and the samples fractured during machining. For the samples belonging to the same group a clear trend was observed: increased time and temperature of the diffusion bonding process resulted in greater thickness of each of the zones at the interface. Fig. 5 illustrates the typical SEM images of each group.

2.3.1. Group A

The structure of most of the samples (*group A*) resembles the structure of sample #3. This group was considered successful. As illustrated in Fig. 5 seven *regions* in total can be distinguished. The chemical composition of the individual sections was evaluated with the WDS and EDS spectroscopies. The WDS concentration profiles of the bonding interface, for the samples of *group A* exhibited a similar pattern to that observed in sample #3 (see figure below):

Starting from the S235 base material (on top), a total of seven different *regions* were identified at the bonding interface (see Fig. 5). *Region I* corresponded to parent material S235 steel. In *region II* black irregularly shaped agglomerations inside the iron matrix were observed. They were composed of titanium carbide. Additionally, vanadium was observed to diffuse from the native titanium alloy, and reversely, manganese diffused from the S235 into titanium. However, both elements were distributed homogeneously. The same agglomerations were reported in the literature by [20,34]; however, those agglomerations were considered by authors as *Kirkendal* voids, due to the different diffusion coefficients of Fe and Ti. Using the typical chemical composition values for each phase given in Table 6, and combining it with the C-Fe-Ti diagram [35], it can be proven, that the agglomerations were formed mainly by titanium carbide.

Regions III and IV corresponded to diffusion interfaces, where direct physical contact between the materials was established. Based on the chemical compositions measured by EPMA (given in Table 6, *region III* was composed primarily of Fe_2Ti intermetallic Laves phase and TiC agglomerations. Noteworthy, for samples bonded at 950°C much lower amount of TiC in the interlayer was observed. Moving towards higher Ti concentration, *region IV* was composed mainly of FeTi. However, the presence of TiC agglomerations, which in some instances exhibited a non-homogeneous distribution, was also noted. As can be seen in Fig. 6, the TiC was observed to be concentrated at the upper boundary of *region IV*.

Region V was one-phase β-Ti region, which was stabilized by the diffusion of iron from S235. The migration of β-stabilizers within the Ti alloy lattice can result in a reduction in the eutectoid transformation temperature of the Ti alloy, so during the diffusion bonding process, the acicular (needle-like) α-β Ti was transformed to a more stable β-Ti phase [20]. Noteworthy, the initial β-phase exhibited the presence of approximately 14 wt-% of V, 1 wt-% of Fe, and 3 wt-% of Al. However, the typical phase composition values, presented in Table 6, demonstrated, around 4 wt-% of V, 16 wt-% of Fe, and 5 wt-% of Al in *region V*. Therefore, the iron substituted vanadium and stabilized the β-Ti phase, which can be also proven by Fe-Ti-V diagram [36], although this diagram is available only for temperatures above 1000°C.

Both *regions VI and VII* were composed of α- and β-Ti. However, *region VI* exhibited a distinctive acicular (*Widmanstätten*) structure, which formed in α+β titanium following the complete transition to β-Ti. This needle-like structure displayed a notable increase in brittleness [21] compared to the initial structure observed in *region VII*. In general, the formation of the *regions V-VII* after the diffusion bonding is a characteristic phenomenon for α+β Ti alloys [37].

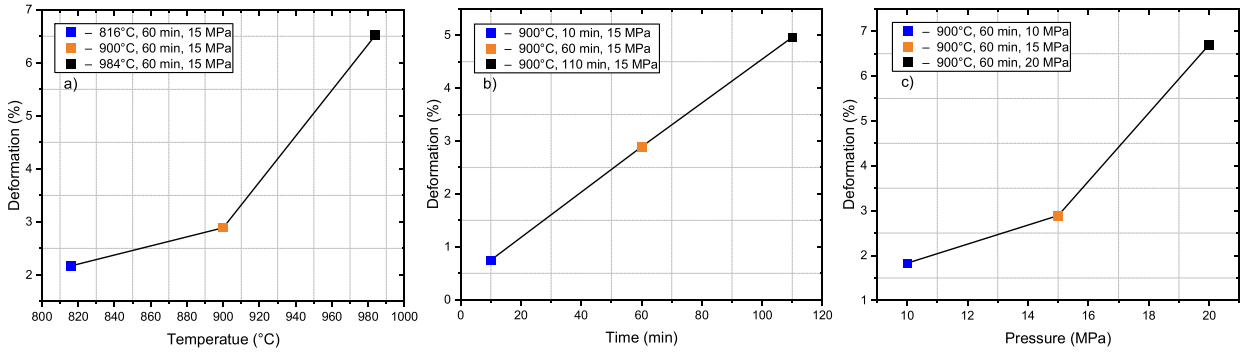

Fig. 3. Dependence of the deformation on DB parameters (a – temperature, b – time, c – pressure), when other parameters are fixed.

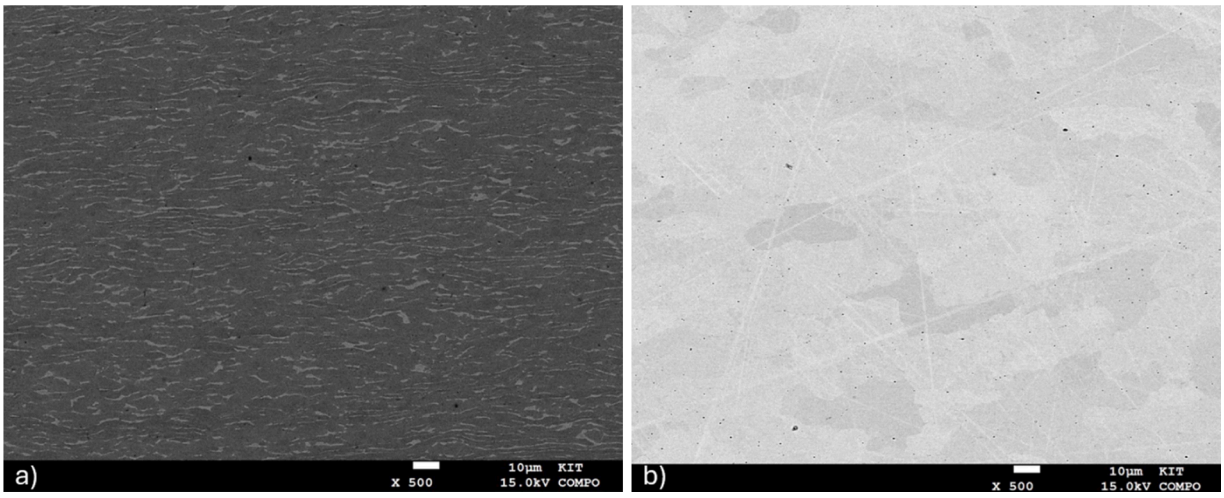

Fig. 4. SEM image of original materials - TiAl6V4 (a) and S235 (b).

Table 4
Chemical composition of the α- and β-phases in TiAl6V4 (wt-%).

Phase/Element	C	Ti	V	Fe	Mn	Al	Total
Light(β)	0.22	81.22	14.47	1.29	0.01	2.78	100.00
Dark(α)	0.20	91.19	3.13	0.05	0.00	5.44	100.00

Table 5
Three groups of SEM images.

Group + Temperatures	A (900°C or 950°C)	B (984°C)	C (850°C)
Sample #	2, 3, 5, 6, 10, 12, 15, 16, 17	8	9, 11, 13, 14

Table 6
Group A – successful joints; Typical (average) chemical and phase compositions of the appropriate *regions*.

	Chemical composition wt-%			
Element	*Region* II	*Region* III	*Region* IV	*Region* V
C	0.90	5.01	3.30	0.48
Al	0.14	0.09	0.70	4.57
Ti	2.45	29.41	50.20	74.82
V	0.22	0.65	1.46	4.43
Mn	0.50	0.20	0.13	0.13
Fe	95.79	64.64	44.25	15.68
Phase composition:	Fe + TiC	Fe_2Ti + TiC	FeTi + TiC	β-Ti

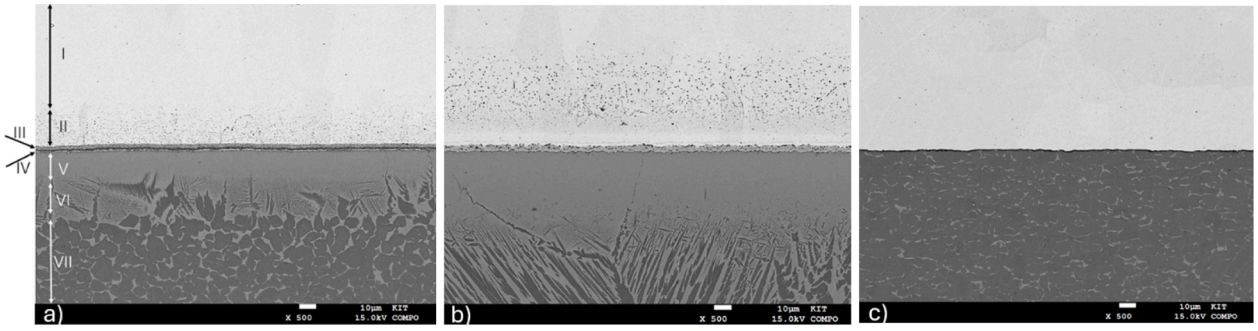

Fig. 5. SEM-BSE-images can be divided into three different groups; *Group A* – sample #3 (a), *group B* – sample #8 (b) and *group C* – sample #11 (c); S235 on the top, TiAl6V4 on the bottom.

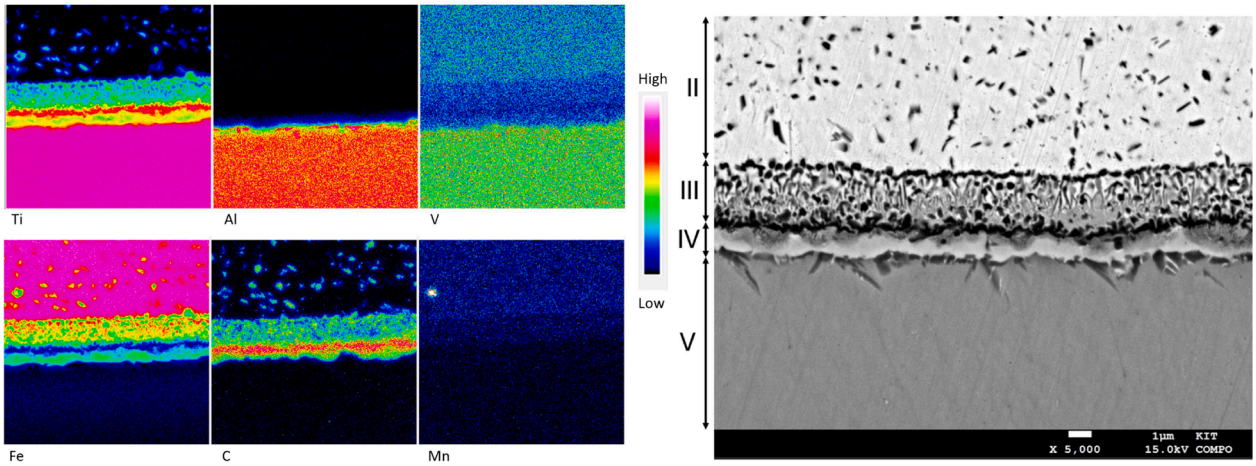

Fig. 6. *Group A* – successful joints; Typical WDS-map of the interface and SEM-BSE image at the same resolution, with *regions* (sample #3).

2.3.2. Group B

Sample #8, the only sample in *group B,* had no *region VII,* (see Fig. 5, in the middle). In the case of this sample, the whole titanium side after cooling was composed of acicular (*Widmanstätten*) structure, resulting from the highest bonding temperature among the whole samples (984°C). In recent works the same result at elevated temperatures was observed [20]. It should be noted that the temperature of the complete transformation (around 900°C) was taken from [38,15], where the values were calculated. Moreover, the measured temperature value in the DB furnace was affected by the position of thermo-couple and the transformation temperature itself was influenced by presence of other elements such as Fe. It can therefore be surmised that the full α- to β-transformation is likely to have occurred only in the case of sample #8.

The WDS concentration profiles of the sample #8 are illustrated in the Fig. 7. The element distribution between the zones was almost the same as for the samples from the *group A*, however the distribution of carbon was observed to be significantly less homogeneous. Consequently, *regions III and IV* in the *group B* were more homogeneous and consisted of almost pure Fe_2Ti and FeTi respectively. From Fig. 7 it can be observed that carbon was concentrated in the black agglomerations. The chemical composition of these agglomerations, as well as of all other *regions,* was measured using EPMA (see Table 7), which corresponds to the TiC + FeTi phase composition. Noteworthy, carbon in smaller concentrations was observed in all phases. According to the C-Fe-Ti diagram [35] it still should appear in the form of TiC, but probably for such low concentrations it was dissolved in Fe, FeTi and Fe_2Ti, and therefore was not observed in SEM-BSE images.

In general, the formation of the acicular structure resulted in increased brittleness, as will be demonstrated in the next section. Therefore, the sample #8 was deemed unsuccessful.

2.3.3. Group C

The entire *group C* comprised samples with unsuccessful bonding. It can be observed from the SEM images in Fig. 5, that no sound bonding between the dissimilar metals was formed. The temperature of the diffusion bonding process for all samples in *group C* was 850°C, which resulted in unsatisfactory bonding. No interdiffusion was observed, as can be seen in the SEM images. Instead, the two initial materials were clearly distinguished. The WDS maps Fig. 8 originate from sample #9:

As previously stated, no acceptable bond was formed between the S235 and the TiAl6V4. However, the samples remained machinable, indicating that a certain level of mechanical strength was achieved, which will be discussed in the subsequent section. It can be concluded, that for *group C* some diffusion processes may have occurred, or a limited degree of micromechanical clamping took place. As illustrated in Fig. 8, an increase in carbon concentration on the surface was observed, indicating the formation of TiC. However, thermodynamic considerations suggest that the temperature of 850°C was too low to form a sound joint.

It is important to emphasize, that the driving force behind the bonding process in this case was not kinetic, but rather thermodynamic, which will be additionally proven in section 2.6. Furthermore, neither the duration of the process, nor the applied pressure had a significant impact on the microstructure, as shown in Fig. 9, which compares SEM images of sample #9 (12 MPa, 850°C, 30 min), sample #13 (12 MPa,

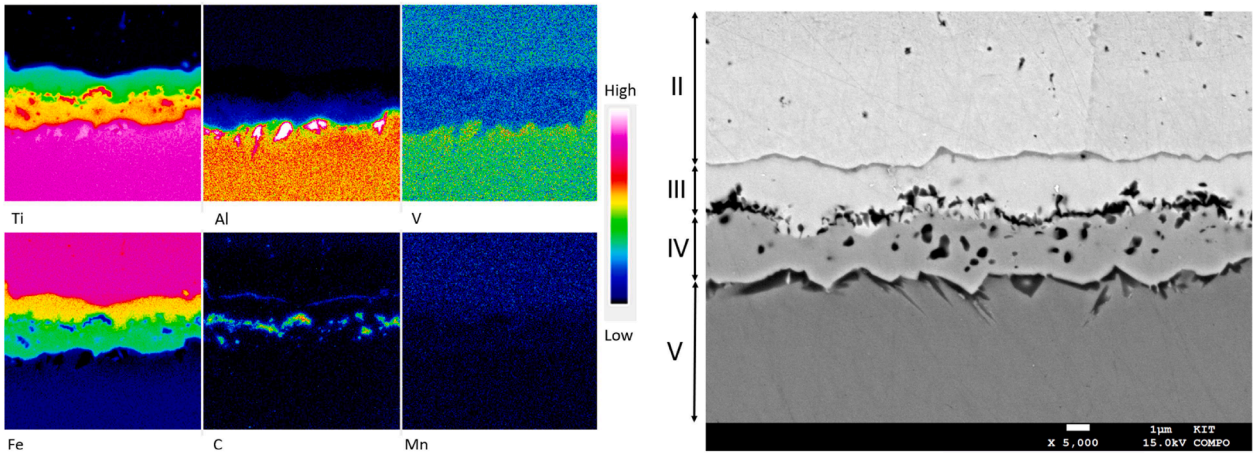

Fig. 7. *Group B* – unsuccessful joint; Typical WDS map of the interface and SEM-BSE image at the same resolution (sample #8).

Table 7
Group B – unsuccessful joint; Typical (average) chemical and phase compositions of the appropriate *regions*.

	Chemical composition wt-%				
Element	*Region* II	*Region* III	*Region* IV	*Region* V	Black Agglomeration
C	0.75	0.66	0.45	0.21	6.63
Al	0.31	0.12	1.20	4.42	0.34
Ti	3.58	27.87	47.39	74.15	59.83
V	0.34	0.78	1.60	4.34	1.60
Mn	0.31	0.32	0.10	0.02	0.15
Fe	94.70	70.26	49.3	16.86	31.45
Phase composition:	Fe + (TiC)	Fe_2Ti + (TiC)	FeTi + (TiC)	β-Ti	FeTi + TiC

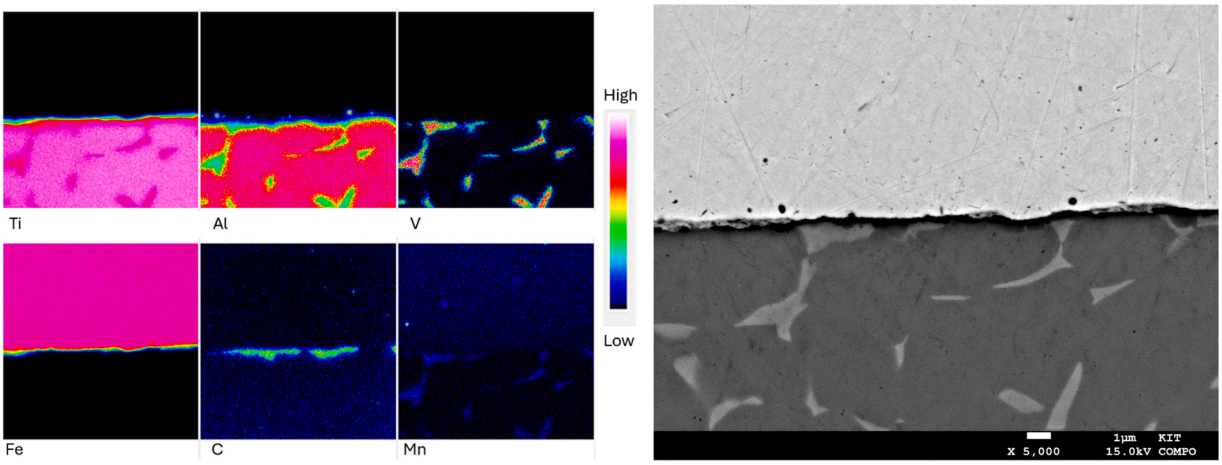

Fig. 8. *Group C* – unsuccessful joints; Typical WDS maps of the interface and SEM-BSE image at the same resolution, with *regions* (sample #9).

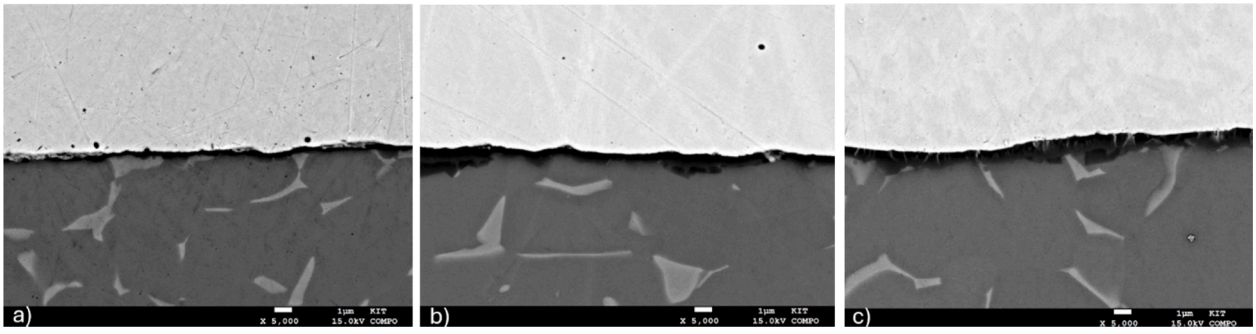

Fig. 9. *Group C* – unsuccessful joints; SEM-BSE comparison of the bonding interface of the sample #9 (a), sample #13 (b) and sample #14 (c).

850°C, 90 min) and sample #14 (18 MPa, 850°C, 90 min).

2.4. Shear strength measurements

The shear strengths of each sample were measured. To decrease the surface pressure, rectangular samples with the dimensions of approximately 6 × 5 × 10 mm^3 were cut. Each sample was subjected to a force gradually increasing until the joint failed (strain rate for all samples was about 0.01 s^{-1}). The shear strength of the joint was determined by dividing the maximum force by the cross-section area. Some of the samples fractured during the machining (sample #7), and therefore no shear strength could be measured. Initially, four measurements were performed for each sample. For some samples (#11, 14, 15), the standard deviation $\left(\mathrm{SD} = \sqrt{\frac{\sum (x-\bar{x})^2}{N-1}}\right)$ value was around 50% of the absolute value, most probably due to just partial bonding (in case of samples #11 and #14) and very weak intermetallic interlayer (sample #15). Consequently, for these samples, six additional measurements were made. Nevertheless, even after that, the standard deviation values for those samples remained high. This effect was observed in samples with relatively low absolute shear strength values, see Table 8 below:

To identify successful samples, only those with a shear strength greater than 200 MPa and standard deviation less than 15% of the absolute value were considered. These samples are highlighted (orange rows) in Table 8.

The results clearly demonstrate that the final shear strength of the samples strongly depended on the temperature. The bonding temperatures of 850°C and 816°C were too low for obtaining the acceptable joint, and 984°C was too high. By contrast, most successful samples were obtained at 900°C, where the time and pressure varied across a wide range but had almost no effect on the shear strength.

2.5. Fracture analysis

Notably, while measuring the shear strength of the samples from the *groups B* and *C,* in all cases the delamination occurred, indicating that,

Table 8
Shear strength values with standard deviation values.

p (MPa)	*T* (°C)	*t* (min)	Sample #	Deformation%	Number of tests	Shear strength (MPa)	SD (MPa)
12	850	30	9	1.49	3	93	46
18	850	30	11	4.81	10	124	66
12	950	30	10	2.54	4	174	21
18	950	30	12	4.76	4	200	10
12	850	90	13	3.67	4	110	32
18	850	90	14	13.02	10	147	84
12	950	90	15	4.32	10	146	52
18	950	90	16	10.89	4	177	22
10	900	60	17	1.83	4	249	33
20	900	60	2	6.70	4	210	10
15	816	60	7	2.17	-	33	-
15	984	60	8	6.52	4	94	42
15	900	10	5	0.75	4	229	23
15	900	110	6	4.96	4	243	11
15	900	60	3	2.89	4	224	10

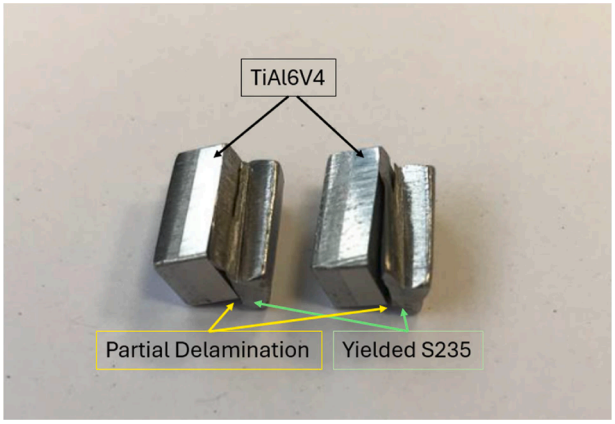

Fig. 10. Group A – Partial delamination and yielding after the shear strength test (sample #3).

the weakest part was the bonding interface. For the *group A*, however (see Fig. 10), for all samples, first the yielding of S235 started (as the contact pressure reached about 500 MPa, indicating that the sample geometry was not ideally chosen) and only after that, the delamination occurred. Since, the yielding of S235 started, the bonded surface was no longer subjected to pure shear stress, complicating the characterisation. Nevertheless, it appears that in this case the fracture had also occurred on the bonding surface, even though the strength was higher than in other *groups*.

Mean thicknesses of each *region* were measured for *group A*, and *group B* (samples from *group C* didn't exhibit any significant diffusion *region*) using SEM images; each region was measured five times, then the average value and SD. Relative thick *regions* (e.g. *II, V* and *VI*) were measured with x500 and x1000 magnification, where *regions III* and *IV* were measured with x5000 magnification. The results are presented in the following Table 9:

The evolution of the intermetallic *regions* (III and IV) is illustrated in Fig. 11. A distinct linear increase in the thickness of both layers was observed with increasing dwell time, while pressure exerted no significant influence. The effect of bonding temperature could not be isolated, as the joint fabricated at 816°C (sample #7) exhibited no detectable diffusion.

Table 9
Thicknesses of each *region* with standard deviation for *groups A* and *B (mean* ± SD).

Sample #	*Region* II	*Region* III	*Region* IV	*Region* V	*Region* VI
2	23.6±1.8	2.5±0.1	1.1±0.1	16.1±0.8	20.8±0.9
3	22.8±0.7	2.6±0.1	1.3±0.1	15.3±1.1	23.6±1.5
5	10.9±0.5	1.8±0.1	0.9±0.1	8.1±0.8	10.1±0.3
6	30.4±0.5	3.1±0.1	1.5±0.2	19.7±0.8	30.8±0.7
8	53.5±1.4	2.5±0.3	3.0±0.2	32.2±1.2	-
10	30.8±0.9	2.6±0.1	1.6±0.2	20.6±0.5	38.1±1.7
12	32.8±1.1	1.8±0.1	1.7±0.1	21.6±0.4	41.0±0.5
15	47.8±1.0	2.1±0.1	2.5±0.1	33.5±0.5	67.4±1.5
16	44.1±1.0	2.0±0.1	2.2±0.1	31.7±0.5	63.9±1.2
17	24.4±0.8	2.6±0.1	1.2±0.1	16.5±0.7	22.7±1.1

No significant correlation was detected between the thickness of the intermetallic layers and the resulting shear strength of the joints. Despite sample #6 having the thickest *region III* layer, its shear strength exceeded 200 MPa. The elevated strength of samples welded at 900°C is likely associated with the presence of TiC, which was significantly reduced in the specimen welded at 984°C (see *region III* and *IV* columns in Table 6 and Table 7). A similar trend was noted for samples welded at 950°C, where the TiC content was lower compared to those bonded at 900°C. Fig. 12 illustrates the differences in intermetallic microstructures for samples welded at 900°C (a) and 950°C (b). Although the samples bonded at 950°C retained the initial α+β distribution on the Ti side (as observed for all samples in *group A*), the composition of regions III and IV more closely resembled that of *group B* (Fig. 7), only few amount of black agglomerations was observed.

2.6. Implementation of the ROCCD

Using the shear strength values, the ROCCD was implemented. For fitting the coefficient values, the least-squares method was applied. Table 10 gives an overview of the most significant parameters, including the *t*-values:

The expression for the dependence of the shear stress on the time, temperature and pressure of the diffusion bonding process was derived as follows:

$$\tau = 224.6 + 4.4p + 23.8T + 0.9t\ - 1.4pT + 1.4pt - 11.4Tt - 3.7p^2 - 62.4T^2 - 1.4t^2, \quad (5)$$

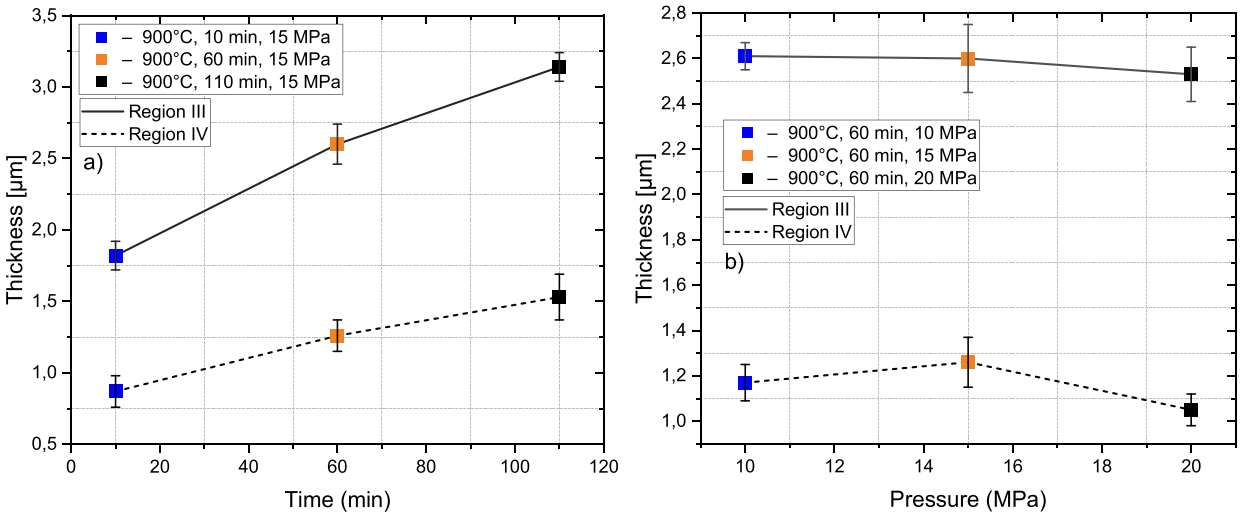

Fig. 11. Dependence of the intermetallic zone's thicknesses on DB parameters (a – time, b – pressure), when other parameters are fixed.

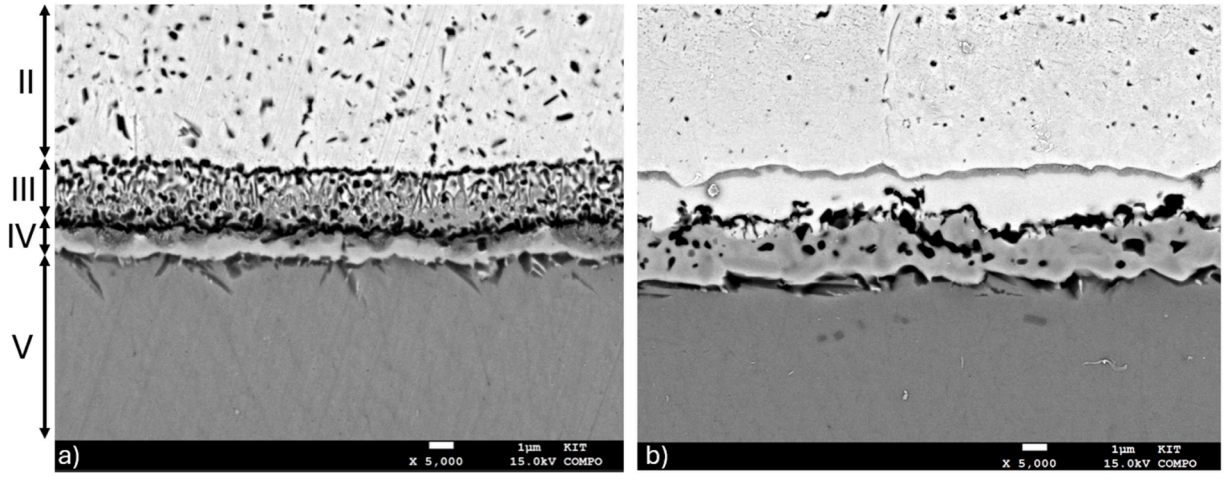

Fig. 12. *Group A* – successful joints; SEM-BSE image at the same resolution, with *regions* for sample bonded at 900°C (sample #3 – a) and at 950°C (sample #15 – b).

Table 10
ANOVA table including the Student's ***t***-statistics; DF – degrees of freedom.

Source	DF	Sum of Squares	F Ratio	Prob > F	Std Error	*t*-ratio	Prob > |*t*|
Intercept	-	-	-	-	6.638	33.850	<.0001
T^2	1	61776.790	155.479	<.0001	5.009	-12.470	<.0001
T	1	7763.927	19.540	0.0007	5.396	4.420	0.0007
Tt	1	1035.125	2.605	0.1305	7.047	-1.610	0.1305
p	1	265.574	0.668	0.4283	5.414	0.820	0.4283
p^2	1	221.478	0.557	0.4686	5.072	-0.750	0.4686
t^2	1	32.337	0.081	0.7799	5.072	-0.290	0.7799
pT	1	15.125	0.038	0.8483	7.047	-0.200	0.8483
pt	1	15.125	0.038	0.8483	7.047	0.200	0.8483
t	1	11.221	0.028	0.8691	5.414	0.170	0.8691

Using the *t*-statistics (95% significance level) non-significant coefficients were removed, and the final expression for uncoded factors was obtained (see Table 10):

$$\tau = 224.6 + 23.8T - 62.4T^2, \quad (6)$$

For uncoded factors:

$$\tau = -20421.4 + 45.4T - 0.025T^2, \quad (7)$$

The expression for coded factors (6) proved our assumption, that dwell time (withing the experimental range) had almost no effect on the joint strength, similar to pressure, whereas the effect of the process temperature was the most significant. This led to the first conclusion, which was, however, already observed in SEM images: the thermodynamics of the process dominates over the kinetics. Which means, that in those parameters' ranges $T \in [816;\ 984]$°C, $p \in [10;\ 20]$ MPa, $t \in [10;\ 110]$ min; it is impossible to avoid the brittle phase formation (initial assumption was, that using the short bonding time will avoid the

intermetallic phase formation). On the other hand, it indicates, that also any pressure in that range is enough (due to TiAl6V4 plasticity under the elevated temperatures) for a diffusion bonding process.

Using the (7), the prediction of the best combination of parameters can be made. By taking the derivative of that equation, the local maximum of the function $\tau(T)$ was found at approximately $T = 908\ ^{\circ}C$, which is close to the condition used for the successful samples # 2, 3, 5, 6, and 17.

As discussed in section 2.1, the ROCCD methodology requires eight replicate experiments at the "zero point." For practical reasons, only one experiment was conducted, assuming that the DB process is sufficiently reproducible. Because this simplification may affect the resulting regression equations, its impact was evaluated as follows. A value of 224 MPa was taken as the mean response at the zero point, and eight additional values were generated using a MATLAB script that sampled from a normal distribution with standard deviations of 5%, 10%, and 20%. For each SD level, 25 iterations were performed. In the 5% and 10% SD conditions, the significance of the model coefficients remained unchanged. At 20% SD, in roughly 44% of iterations (those containing values beyond 2σ or close to that threshold), the linear temperature term (T) became insignificant, while the quadratic term (T^2) remained significant, confirming that bonding temperature still exerts the strongest effect on the response. This confirms that the initial simplification has a negligible effect on the final model.

3. Discussion

The compositions of each *region* showed qualitatively with WDX and measured quantitatively with SEM-BSE were in accordance with theory: the concentration profile of the diffusion zone in a multi-phase case led to the formation of bands, where the appropriate bands composition corresponded to the phase-diagrams of the system. Even though the phase diagram for the mixture of six elements present in this study was not available, most of the elements had quite low concentrations (C, Al, V, Mn). By comparing the phase diagrams of those elements, only carbon, even at small concentrations does not dissolve in Ti, forming TiC agglomerations, which were observed. Other elements diffused through different *regions* relatively homogeneously.

As was mentioned earlier in section 2.3, carbon, even in small concentrations, leads to the TiC formation [35]. It is likely that the homogeneous distribution of the TiC in *group A* (900°C) helped to increase the mechanical strength [39], which was responsible for the success of the joints in that group. Aluminium, according to the phase diagram [40] (available only for temperatures above 900°C), in small concentrations mixes readily with Ti and Fe. A similar effect can be observed in the case of vanadium [36] (with the phase diagram is available only above 1000°C). The Fe-Mn-Ti diagram was only available for low concentrations of Ti, but from both Ti-Mn [41] Fe-Mn [42], for such low concentrations of Mn ($<$ 1%), manganese did not affect the phase composition of the joint. Multiple diffusion regions formed during the experiments, but despite measuring the thickness of each *region*, no relationship with shear strength was identified. The presence of TiC within the intermetallic layer was found to enhance joint strength, although the fracture behaviour remained brittle. For the sample #8 bonded at 984°C, acicular structure formation in Ti-side was observed. This indicates that only in this sample the complete $\alpha + \beta \rightarrow \beta$ transformation occurred. Afterwards, during cooling α phase started to precipitate again on specific crystallographic planes within the β grains. Although the needle structure is more brittle than the initial TiAl6V4 microstructure, delamination occurred at the intermetallic interface. The strength of this interface is lower, than for the joints from *group A*, which can be explained by absence of TiC on the bonding surface. A similar, but less pronounced effect for samples welded at 950°C was observed.

Given that the observed strengths were already near their practical maximum, additional refinement of the bonding parameters is unlikely to produce substantial gains. Moreover, the measured shear strengths were already close to the upper limit for this material system, suggesting that further optimization of the diffusion bonding parameters is unlikely to yield significant improvements.

The best result, however, albeit with a higher standard deviation, was achieved for the sample bonded 60 min at 900°C with a bonding pressure of 10 MPa, which is very close to the analysis made in [26,29] for TiAl6V4/AISI304 material pair. *Mo* et al. in the review paper for the pair TiAl6V4/Stainless steel also reported very similar values for the process time and temperature, however, in a relatively big range. That is also supported by [10], where the ultimate shear strength values for the joint of the mild steel (S355) and Inconel were almost the same, even though the material combination in all cases was different. It was shown, that even at 950°C relatively high strength of the joint can be obtained (200 MPa, sample #12). However, increasing the dwell time led to the significant diffusion of TiC from intermetallic zones, reducing the strength of the joint.Assuming that the ultimate tensile strength for the TiAl6V4 is around 950 MPa, and for the S235 the value can vary from 350 to 600 MPa, the ultimate shear strength, assuming the *von Mises* yield criterion [43], for TiAl6V4 and S235 should be 548 MPa and 200-345 MPa respectively. Assuming the *Tresca* criterion [43], however, the values of the strengths would be even lower. As outlined in the introduction section, the primary motivation for investigating the diffusion bonding of the S235/TiAl6V4 material pair lies in its prospective use in axially laminated rotors for synchronous reluctance machines. The results presented in this work offer quantitative guidance for the manufacturing of S235/TiAl6V4 laminated composites. The optimized bonding conditions and the validated material combination provide a foundation for the development of lightweight, high-strength rotors. Nevertheless, the inherently brittle fracture behaviour of the joint, together with the pronounced mismatch in the thermal expansion coefficients of the two materials, may introduce additional complications when implemented in an operational rotor. Moreover, in the context of industrial-scale rotor fabrication, several challenges can be anticipated:

- Difficulties in scaling up to complex geometries due to the creep tendency of TiAl6V4.
- Macroscopic deformation of the TiAl6V4 layers, which may hinder microscopic diffusion.
- Non-uniform heating of large billets, potentially leading to inferior bonding in the billet core—precisely the region subjected to the highest stresses in a solid rotor.
- Challenges in integrating the process into existing manufacturing routes, including the potential inability to produce large numbers of billets simultaneously.

4. Conclusion

In this paper, the influence of diffusion bonding parameters on the shear strength of ALA composites between magnetic steel S235 and TiAl6V4 was systematically investigated. The design of experiment method was used to understand how the diffusion bonding parameters influence the joint strength. The main conclusions are:

- Magnetic mild steel S235 and TiAl6V4 were found as promising candidates for an axially laminated rotor in high-speed synchronous reluctance machines.
- Thermodynamics dominates over kinetics during diffusion bonding of TiAl6V4/S235, leading to microstructural evolution that controls joint strength.
- No correlation was observed between intermetallic layer thickness and shear strength, whereas specimens with TiC-containing interlayers exhibited the highest strength.
- The general regression model describing the effect of time, temperature and pressure on the shear strength of the joint was constructed.

- The dwell time and contact pressure were insignificant in the range $p \in [10, 20]$ MPa, $t \in [10, 110]$ min, although this depends on sample geometry and may vary for larger billets.
- The ultimate shear strength of around 249 MPa was reached, which is most likely the limit for this material combination.

The successful joints between the TiAl6V4 and S235 were achieved, however the strength of the joint was limited by the intrinsic strength of the mild steel. Future work will therefore focus on the fabrication and testing of an axially laminated rotor prototype employing this material combination or, alternatively on the identification of magnetic materials with higher mechanical compatibility with TiAl6V4.

AI tools statement

During the preparation of this work, the author(s) used DeepL and ChatGPT to improve the readability. The author(s) reviewed and edited the content and take full responsibility for the publication.

CRediT authorship contribution statement

Fedor Levchenko: Writing – review & editing, Writing – original draft, Visualization, Methodology, Investigation, Data curation, Conceptualization. **Thomas Gietzelt:** Writing – review & editing, Supervision, Resources, Methodology. **Eero Scherman:** Writing – review & editing, Writing – original draft, Investigation, Data curation. **Uta Gerhards:** Formal analysis, Data curation. **Volker Toth:** Resources. **Juha Pyrhönen:** Writing – review & editing, Supervision, Project administration, Funding acquisition. **Martin Doppelbauer:** Writing – review & editing, Supervision, Project administration, Funding acquisition.

Declaration of competing interest

The authors declare the following financial interests/personal relationships which may be considered as potential competing interests:

Fedor Levchenko reports was provided by European Union. If there are other authors, they declare that they have no known competing financial interests or personal relationships that could have appeared to influence the work reported in this paper.

Acknowledgements

This work was funded by the European Union through Marie Sklodowska-Curie Actions under Grant ID101072580 – HIPO.

Supplementary materials

Supplementary material associated with this article can be found, in the online version, at doi:10.1016/j.rineng.2026.109642.

Data availability

Data will be made available on request.

References

[1] P. Ramesh, N.C. Lenin, High power density electrical machines for electric vehicles—comprehensive review based on material technology, IEEE Trans. Magn. 55 (11) (2019) 1–21, https://doi.org/10.1109/TMAG.2019.2929145.
[2] Y. Gong, et al., Improvement of the mechanical strength of high speed synchronous reluctance machines by fiber reinforced support structures, in: 2022 International Conference on Electrical Machines (ICEM), 2022, pp. 49–55, https://doi.org/10.1109/ICEM51905.2022.9910716.
[3] G.V. Konushkov, B.M. Zotov, E.I. Merkin, Ferrites and their joints with metals and ceramics, in: Г.В. Конюшков, Б.М. Зотов, Э.И. Меркин (Eds.), Ферриты и Их Соединения с МеталлаМи и КераМикой, Москва, 'Энергия', 1979, Energy, Moscow, 1979.
[4] A. Credo, E. Kurvinen, I. Petrov, E. Scherman, J. Sopanen, J. Pyrhönen, Materials applicable to an axially-laminated synchronous reluctance machine considering mechanical and electromagnetic aspects, IEEE Trans. Ind. Appl. 60 (1) (2024) 153–163, https://doi.org/10.1109/TIA.2023.3309285.
[5] S. Kang, L. Kong, X. Zhuo, Z. Sun, Y. Li, Y. He, Study on the machining performance of Ti6Al4V titanium alloy by negative polarity Near-dry electrical discharge milling, Results Eng. 28 (2025) 108429, https://doi.org/10.1016/j.rineng.2025.108429.
[6] R.R. Kumar, R.K. Gupta, A. Sarkar, M.J.N.V. Prasad, Vacuum diffusion bonding of α-titanium alloy to stainless steel for aerospace applications: interfacial microstructure and mechanical characteristics, Mater. Charact. 183 (2022) 111607, https://doi.org/10.1016/j.matchar.2021.111607.
[7] I. Tomashchuk, D. Grevey, P. Sallamand, Dissimilar laser welding of AISI 316L stainless steel to Ti6–Al4–6V alloy via pure vanadium interlayer, Mater. Sci. Eng. A 622 (2015) 37–45, https://doi.org/10.1016/j.msea.2014.10.084.
[8] H.S. Lee, K.J. Min, Development of diffusion welding process for high temperature materials, Key Eng. Mater. 689 (2016) 3–6, https://doi.org/10.4028/www.scientific.net/KEM.689.3.
[9] V. Abramenko, J. Nerg, I. Petrov, J. Pyrhönen, Influence of magnetic and nonmagnetic layers in an axially laminated anisotropic rotor of a high-speed synchronous reluctance motor including manufacturing aspects, IEEE Access 8 (2020) 117377–117389, https://doi.org/10.1109/ACCESS.2020.3004705.
[10] E. Scherman, E. Sikanen, H.K. Yeddu, M. Amraei, J. Sopanen, Microstructure and mechanical properties of steel and ni-based superalloy joints for rotors of high-speed electric motors, Materials 15 (19) (2022) 19, https://doi.org/10.3390/ma15196906. Art. no.
[11] L. Nipa, H.R. Siller, M. Sharma, B. Rout, R.A. Mirshams, Investigating the effects of hot isostatic pressing and proton irradiation on L-PBF stainless steels via nanoindentation across different strain rates, Results Eng. 27 (2025) 106637, https://doi.org/10.1016/j.rineng.2025.106637.
[12] P. Klima, J. Barta, D. Koutny, O. Vitek, High-speed synchronous reluctance machine rotor using multi-material additive manufacturing, IEEE Trans. Energy Convers. (2024) 1–10, https://doi.org/10.1109/TEC.2024.3475512.
[13] R. Wrobel, B. Mecrow, A comprehensive review of additive manufacturing in construction of electrical machines, IEEE Trans. Energy Convers. 35 (2) (2020) 1054–1064, https://doi.org/10.1109/TEC.2020.2964942.
[14] A.A. Noman, M.S. Shaari, H. Mehboob, A.H. Azman, Recent advancements in additively manufactured hip implant design using topology optimization technique, Results Eng. 25 (2025) 103932, https://doi.org/10.1016/j.rineng.2025.103932.
[15] H. Wang, N. Warnken, R.C. Reed, Thermodynamic and kinetic modeling of bcc phase in the Ti–Al–V ternary system, Mater. Sci. Eng. A 528 (2) (2010) 622–630, https://doi.org/10.1016/j.msea.2010.09.013.
[16] J. Chipman, Thermodynamics and phase diagram of the Fe-C system, Metall. Trans. 3 (1) (1972) 55–64, https://doi.org/10.1007/BF02680585.
[17] Chapter 7 - diffusional transformations, in: S. Banerjee, P. Mukhopadhyay (Eds.), Pergamon Materials Series, Pergamon Materials Series, 12, Phase Transformations, Pergamon, 2007, pp. 555–716, https://doi.org/10.1016/S1470-1804(07)80060-5.
[18] A. V. Lyushinskij and E. S. Fedorova, 'Diffusion welding method', RU 2 720 267 C1, 2020.
[19] C. Velmurugan, V. Senthilkumar, S. Sarala, J. Arivarasan, Low temperature diffusion bonding of Ti-6Al-4V and duplex stainless steel, J. Mater. Process. Technol. 234 (2016) 272–279, https://doi.org/10.1016/j.jmatprotec.2016.03.013.
[20] S. Kundu, S. Sam, S. Chatterjee, Evaluation of interface microstructure and mechanical properties of the diffusion bonded joints of Ti–6Al–4V alloy to micro-duplex stainless steel, Mater. Sci. Eng. A 528 (15) (2011) 4910–4916, https://doi.org/10.1016/j.msea.2011.02.050.
[21] H. Li, M. Li, H. Liu, C. Zhang, Effect of grain size of primary α phase on bonding interface characteristic and mechanical property of press bonded Ti–6Al–4V alloy, Trans. Nonferrous Met. Soc. China 26 (1) (2016) 93–99, https://doi.org/10.1016/S1003-6326(16)64093-1.
[22] H. Zhang, J. Li, P. Ma, J. Xiong, F. Zhang, Study on microstructure and impact toughness of TC4 titanium alloy diffusion bonding joint, Vacuum 152 (2018) 272–277, https://doi.org/10.1016/j.vacuum.2018.03.019.
[23] S. Kundu, S. Chatterjee, Characterization of diffusion bonded joint between titanium and 304 stainless steel using a Ni interlayer, Mater. Charact. 59 (5) (2008) 631–637, https://doi.org/10.1016/j.matchar.2007.05.015.
[24] D. Mo, et al., A review on diffusion bonding between titanium alloys and stainless steels, Adv. Mater. Sci. Eng. 2018 (1) (2018) 8701890, https://doi.org/10.1155/2018/8701890.
[25] A.V. Lavrishchev, et al., Investigation of the solid-phase joint of VT-14 titanium alloy with 12KH18N10T stainless steel obtained by diffusion welding through intermediate layers, Metals 11 (8) (2021) 1325, https://doi.org/10.3390/met11081325.
[26] A. Negemiya, R. Selvarajan, T. Sonar, Effect of diffusion bonding time on microstructure and mechanical properties of dissimilar Ti6Al4V titanium alloy and AISI 304 austenitic stainless steel joints, Mater. Test. 65 (1) (2023) 77–86, https://doi.org/10.1515/mt-2022-0209.
[27] T.F. Song, et al., Microstructure and mechanical properties of vacuum diffusion bonded joints between Ti-6Al-4V titanium alloy and AISI316L stainless steel using Cu/Nb multi-interlayer, Vacuum 145 (2017) 68–76, https://doi.org/10.1016/j.vacuum.2017.08.017.
[28] A. Arun Negemiya, S. Rajakumar, V. Balasubramanian, Diffusion bonding of a titanium alloy to austenitic stainless steel using copper as an interlayer, SN Appl. Sci. 1 (9) (2019) 1128, https://doi.org/10.1007/s42452-019-1189-6.

[29] A. Arun Negemiya, S. Rajakumar, V. Balasubramanian, Optimization of Ti-6Al-4V/AISI304 diffusion bonding process parameters using RSM and PSO algorithm, Multidiscip. Model. Mater. Struct. 15 (6) (2019) 1037–1052, https://doi.org/10.1108/MMMS-07-2018-0134.
[30] T. Gietzelt, V. Toth, A. Huell, R. Dittmeyer, Determining the dependence of deformation during diffusion welding on the aspect ratio using samples made of SS 304 (1.4301), Adv. Eng. Mater. 19 (2) (2017) 1600344, https://doi.org/10.1002/adem.201600344.
[31] G.E.P. Box, J.S. Hunter, Multi-factor experimental designs for exploring response surfaces, Ann. Math. Stat. 28 (1) (1957) 195–241.
[32] A.M. Dean, D. Voss, Design and Analysis of Experiments, Springer Science & Business Media, 2000, https://doi.org/10.1007/978-3-319-52250-0 [Online]. Available.
[33] L. Badea, M. Surand, J. Ruau, B. Viguier, Creep behavior of Ti-6Al-4V from 450°C to 600°C, Univ. Polytech. Buchar. Sci. Bull. Ser. B Chem. Mater. Sci. 76 (n 1) (2014) 185–196.
[34] S. Kundu, S. Sam, S. Chatterjee, Interface microstructure and strength properties of Ti–6Al–4V and microduplex stainless steel diffusion bonded joints, Mater. Des. 32 (5) (2011) 2997–3003, https://doi.org/10.1016/j.matdes.2010.12.052.
[35] V. Raghavan, C-Fe-Ti (carbon-iron-titanium), J. Phase Equilib. 24 (1) (2003) 62–66, https://doi.org/10.1007/s11669-003-0010-8.
[36] V. Raghavan, Fe-Ti-V (iron-titanium-vanadium), J. Phase Equilib. Diffus. 32 (4) (2011) 381–382, https://doi.org/10.1007/s11669-011-9895-9.
[37] D. Mo, et al., A review on diffusion bonding between titanium alloys and stainless steels, Adv. Mater. Sci. Eng. 2018 (1) (2018) 8701890, https://doi.org/10.1155/2018/8701890.
[38] V. Raghavan, Al-Ti-V (aluminum-titanium-vanadium), J. Phase Equilib. Diffus. 26 (3) (2005) 276–279, https://doi.org/10.1007/s11669-005-0118-0.
[39] H. Wu, S. Huang, H. Zhu, Z. Xie, Strengthening FeCrNiCu high entropy alloys via combining V additions with in-situ TiC particles, Scr. Mater. 195 (2021) 113724, https://doi.org/10.1016/j.scriptamat.2021.113724.
[40] V. Raghavan, Al-Fe-Ti (aluminum-iron-titanium), J. Phase Equilib. 23 (4) (2002) 367, https://doi.org/10.1361/105497102770331613.
[41] J.L. Murray, The Mn−Ti (manganese-titanium) system, Bull. Alloy Phase Diagr. 2 (3) (1981) 334–343, https://doi.org/10.1007/BF02868287.
[42] O.K. von Goldbeck, 'Iron—manganese Fe—Mn', in: O.K. von Goldbeck (Ed.), IRON—Binary Phase Diagrams, Springer, Berlin, Heidelberg, 1982, pp. 61–63, https://doi.org/10.1007/978-3-662-08024-5_38.
[43] S. Chatti, L. Laperrière, G. Reinhart, T. Tolio, CIRP Encyclopedia of Production Engineering, Springer, 2019, https://doi.org/10.1007/978-3-662-53120-4. Accessed: Jan. 22, 2025. [Online]. Available.